AIAA JOURNAL
Vol. 49, No. 8, August 2011

Simulation of Helicopter Community Noise in Complex Urban Geometry

Damiano Casalino,* Mattia Barbarino,† and Antonio Visingardi†
Italian Aerospace Research Center, 81043 Capua, Italy

DOI: 10.2514/1.J050774

The problem of helicopter noise generation, fuselage scattering, and propagation in an urban environment is solved using a wave-splitting technique based on a coupled Ffowcs Williams and Hawkings and finite element method computation. This original technique allows the forward and backward propagation of the noise generated by a rotating device through a computational domain in the presence of reflecting obstacles, both in the source region and in the far field. The acoustic pressure on the boundaries of two overlapping chimera grids are computed in the time domain using the Ffowcs Williams and Hawkings analogy and are used to prescribe jump conditions across the chimera interface. The coupled Ffowcs Williams and Hawkings and finite element method technique is verified only for wave propagation in a quiescent medium, but the proposed formulation can take into account the convective effects associated with a flow medium. To reduce the computational time required to compute the noise signals on the chimera interface, a fast rotor noise model is used that consists of replacing the blade with a wedge of equivalent sectional area and equivalent unsteady aerodynamic action on the fluid. The fast rotor noise model is verified and validated in helicopter blade–vortex interaction conditions and constitutes the second original contribution of this work.

Nomenclature

c = speed of sound
i = imaginary unit ($\sqrt{-1}$)
k = acoustic wave number (ω/c_a)
l = blade chord
$\mathbf{n}$ = normal unit vector
R = rotor radius
T = mean-flow temperature
$\mathbf{U}$ = mean-flow velocity
ξ, η, ζ = finite element method shape functions
ρ = mean-flow density
ϕ = acoustic velocity potential
ω = radian frequency
$\sim$ = dimensionless mean-flow quantities

Subscript

a = atmospheric ambient quantities

I. Introduction

ONE of the emerging problems in helicopter operations in urban areas is the prediction of the noise impact on buildings and its indoor transmission. Indeed it is well recognized that low frequency and impulsive noise has a higher psychological impact on the majority of the population compared with higher-frequency noise of equal loudness. A research carried out in 2005 by the University of Salford [1] on the assessment of low-frequency-noise complaints concluded that 5 dB was an appropriate penalty for fluctuating low-frequency sound. The higher impact of helicopter noise is also associated with the so-called virtual noise effects (such as, for instance, the induced fear for safety) and with the building vibration. While most of the psychological effects are mitigated by the habitual exposure and may be biased by socioeconomic factors, the building vibration is an objective annoyance factor that can only be addressed at the level of architectural design [2]. This is a key aspect for the acoustic insulation of buildings around heliports and, in particular, schools, for which the World Health Organization recommends a maximum equivalent indoor level of background noise not exceeding 35 dBA, which is 15 dBA below the average voice level.

Another domain in which the prediction of outdoor/indoor noise propagation and transmission could have an important role in the future is the design of military ships. It is well recognized that sailors living and working aboard navy ships are exposed to numerous noise sources on deck and throughout the ship that exceed safe limits. A recent study by the U.S. Centers for Naval Analyses [3] demonstrated a clear correlation between long-term assignment aboard surface warships and an increased rate of hearing loss. In 2004 the U.S. Veterans Administration spent $108 million in disability payments for hearing loss to 15,800 U.S. Navy personnel. The technological interest in shipboard noise mitigation through passive/active acoustic treatments and suitable architectural design is self-evident; in the case of shipboard helicopters, it is not only a military concern.

This paper addresses a specific problem in the field of helicopter computational aeroacoustics (CAA): the prediction of the near-field fuselage noise scattering effects and the far-field wave reflections due to obstacles. A possible approach to deal with the fuselage scattering problem consists of solving an integral equation through a boundary element method (BEM) discretization for the full unsteady aerodynamic field around the rotor and the fuselage or for the scattered acoustic field, typically in frequency domain, by prescribing the incident acoustic field on the fuselage [4]. The incident acoustic pressure can be computed using the Ffowcs Williams and Hawkings (FW-H) analogy applied to the isolated rotor [5]. A similar idea has been also used recently by Schram et al. [6] to investigate the installation effects of low-speed ducted fans.

Because of computational constraints and modeling limitations, the direct integral approach, as well as the coupled FW-H/BEM approach, are not suited to take into account the mean-flow refraction effects. An alternative to the BEM solution consists of solving a convective wave equation. In this case 2 methods are used to prescribe the aeroacoustic sources. The first one consists of solving the wave equation for the scattered acoustic field, and the second one consists of prescribing a rotor equivalent distribution of volume sources [7]. The approach presented in this paper combines these two methods: in the near field a finite element method (FEM) problem is

---

Presented at the 16th AIAA/CEAS Aeroacoustics Conference, Stockholm, Sweden, 7–9 June 2010; received 15 July 2010; revision received 30 November 2010; accepted for publication 13 March 2011.

*Research Engineer, Aerodynamics and Aeroacoustics Laboratory. Member AIAA.

†Research Engineer, Aerodynamics and Aeroacoustics Laboratory.

solved for the scattered acoustic pressure with the incident acoustic pressure prescribed on the fuselage, while in the far-field a FEM problem is solved for the overall acoustic pressure. The near- and far-field problems are solved on two overlapping grids, with a jump condition specified on the grid interfaces. Both the jump and the fuselage boundary conditions involve the acoustic pressure and its gradient computed by using a FW-H analogy applied to the isolated rotor. The idea of introducing rotating noise sources into the FEM computational domain through a surface jump condition is somehow original, although the use of surface distribution of singularities is a well established mathematical technique in the field of aerodynamics and aeroacoustics [8].

One of the ultimate goals of the present research is the capability to compute the noise generated and radiated by a helicopter in takeoff and landing conditions in proximity of the deck of a ship, taking into account the aerodynamic and aeroacoustic interactional effects. As a preliminary step, the coupled FW-H/FEM method is verified only in the case of sound propagation in a quiescent fluid, a situation in which a coupled FW-H/BEM method would lead to the same acoustic results. It is worthy to mention that the problem of helicopter noise generation and propagation involving strong proximity effects from nearby ground introduces several modeling complexities in the unsteady aerodynamic part. Although this problem is the object of a fervent research [9–11], it is not in the scope of the present work.

A drawback of the coupled FW-H/FEM model is the necessity to compute the noise generated by the rotor at all the points of the fuselage and the chimera interface. Even for the lowest blade-passage harmonics this yields to several thousands of computational points, thus resulting in unacceptable computational times. A fast rotor noise (FRN) model developed in the framework of helicopter trajectory optimization is used to reduce the FW-H computational time, while preserving an adequate level of accuracy. The model is based on the classical spanwise compact dipole model, integrated with an original compact monopole model to take into account the blade-thickness effects. The thickness noise contribution is shown to improve the accuracy of the near- and far-field rotor noise prediction compared with the compact dipole model.

The paper is structured in the following way. In Sec. II the numerical tools used in the present work are shortly described. In Sec. III the FW-H/FEM coupling technique is presented and verified for a simple prototype problem. The FRN model is presented in Sec. IV, and it is validated against experimental data for a helicopter in blade–vortex interaction conditions in Sec. V. Furthermore, the noise computed using the coupled FW-H/FEM method in the absence of any reflecting obstacle is compared with the noise computed using the FW-H analogy and the same unsteady blade pressure distribution. To demonstrate the capabilities of the method, the noise field in the presence of buildings is computed for the first two blade-passage harmonics and qualitative results are reported in Sec. VI. Finally, the main outcomes of the present work are summarized in Sec. VII.

II. Description of the Numerical Tools

The computational tools used in the present work are based on well established numerical techniques whose description is not in the scope of the present work. However, some relevant key elements of the formulation and software implementation are provided, while further details can be found in the references.

The first element of the computational chain is the unsteady aerodynamic code. This computes the pressure on the rotor blades due to the blade motion and to the blade–vortex interactions occurring in the prescribed flight conditions. The Italian Aerospace Research Center (CIRA) code RAMSYS [12] (Rotorcraft Aerodynamic Modeling System) is used, which is an unsteady BEM solver for multibody configurations based on Morino's boundary integral formulation [13]. For the sake of the present analysis, the Laplace equation for the velocity potential is solved in a free-wake modality following the approach proposed by Gennaretti and Bernardini [14] to deal with the wake interaction with the rotor blades and the helicopter fuselage. Following the classical unsteady aerodynamic theories, the effect of the flow incompressibility assumption on the prediction of the blade unsteady forces is negligible when the travel time over the blade chord of the acoustic fluctuation generated by the flow unsteadiness is smaller than the characteristic unsteadiness time, in other words, when the blade is acoustically compact in the chordwise direction ($kl < 1$). This simple criterion establishes an upper bound for the BPF harmonic order N_H, i.e $N_H < R/l$. In the present study, the rotor radius–chord ratio is $R/l = 18.2$ and we have considered only the first two harmonics.

The second element of the computational chain is the FW-H code. This integrates the blade pressure fluctuations provided by RAMSYS to compute the pressure fluctuations in the time domain at chimera interface and fuselage nodes. The CIRA code $Opty\partial B^{\mathrm{FWH}}$ is used, which is based on the forward time solution of formulation 1A by Farassat and Succi [15], as described in [16]. The code has been recently developed in order to overcome some limitations of similar codes written in the past by the lead author and others at CIRA. The main novel functionalities of $Opty\partial B^{\mathrm{FWH}}$ that are exploited in the present work are shortly described.

1) Multibody kinematics are supported, and the surface velocity required by the FW-H formulation is computed by finite difference of transient grids [transient computational fluid dynamics (CFD) solution files] in the case of complex body motion.

2) The integration surface can be rigid or deformable, and the variation of the surface cell size is taken into account by the Gaussian integration.

3) The signal reconstruction in the forward time is carried out at the end of the computation by projecting the nonconstant time-step solution on a constant time-step series.

The third and last element of the computational chain is the FEM code. This computes the acoustic propagation in the frequency domain within the inner and the outer domains, coupled through a jump condition at the chimera interface. The CIRA code $Opty\partial B$ is used, which is based on the continuous Galerkin discretization proposed by Astley and Eversman [17]. The jump condition at the chimera interface is computed using the time Fourier components of the pressure signals provided by $Opty\partial B$. The implementation of the jump condition and chimera coupling technique is made easier by a flexible management of the boundary conditions. This consists of adding to the unknowns vector of the FEM model the normal derivatives of the acoustic variables at all the boundary nodes. Hence, the boundary-condition matrix is computed separately from the field matrix, the overall linear system is assembled for a specific value of k, and it is solved using either iterative or direct solvers. Details about the physical models employed in the code can be found in [18].

III. FW-H/FEM Chimera Coupling Technique

For the reasons discussed in the introduction, the propagation model selected for the present study is a convected wave equation for the acoustic potential solved in the frequency domain through a FEM discretization. In acoustic propagation problems the noise sources can be introduced through boundary conditions or field sources: i.e., terms at the right-hand side of the wave equation. The boundary-condition approach is generally limited to the case of sources outside the propagation domain: for instance, fan-noise propagation problems [19]. In the case of sources inside the propagation domain, the use of an internal boundary condition around the source is rigorous only in the absence of wave backscattering. This is because the boundary condition prescribes the acoustic wave entering the computational domain, but cannot be crossed by an impinging wave from the computational domain without generating a spurious reflection. The source field approach is generally limited to nonmoving sources: for instance, airframe-noise propagation problems [20]. A combination of these two approaches is proposed in the present work, which consists of using an equivalent source distribution over a surface around the helicopter that splits the propagation problem into an inner and an outer problem, coupled by a jump boundary condition. The jump condition is computed considering the actual source of noise in the absence of any obstacle. In the present study, the jump condition is computed by applying a FW-H analogy to the unsteady pressure distribution over the rotor blades. More generally, the jump condition can be provided by a compressible unsteady CFD analysis.

The coupled FW-H/FEM technique is based on the idea that instead of prescribing the value of pressure and its normal derivative on a closed surface, as required by the Kirchhoff theorem to ensure the uniqueness of the solution, a jump of pressure and its normal derivative is prescribed on the interface between two adjacent grids. In the inner grid a propagation problem is solved for the scattered waves, while in the outer grid a propagation problem is solved for the incident and scattered waves. Both problems are solved using a FEM discretization in the frequency domain, while the jump conditions are computed using the FW-H analogy in the time domain.

The wave model employed is the one revised by Pierce [21], describing the propagation of potential fluctuations superimposed to a rotation mean flow that varies slowly over the length and time scales of the sound waves (high-frequency limit). Details about this equation and its limits of validity can be found in [18,22,23]. In the following, the wave equation is denoted as $\mathcal{L}(\phi; k, \tilde{\mathbf{U}}, \tilde{\rho}, \tilde{T}) = 0$, while the relationship between the acoustic pressure and acoustic potential is $p = \rho_a c_a \tilde{\rho}(ik\phi - \tilde{\mathbf{U}} \cdot \nabla\phi)$.

Although the present method allows the noise generated by a rotating device to be input into a frequency-domain CAA simulation, it cannot take into account Doppler effects associated with the relative motion between the sources in the inner domain and the obstacles in the outer domain. This limitations reduce the applicability of the present approach to cases for which the flight distance over one acoustic period is sufficiently small compared with a characteristic dimension of the problem.

For the sake of its practical generality, the coupled FW-H/FEM technique has been developed for two overlapping grids in a so-called chimera modality. Therefore, the grid interfaces at which the jump conditions must be prescribed are two, as illustrated in Fig. 1. The red and black lines in the sketch denote the boundaries of the inner (labeled 1) and outer (labeled 2) problems, respectively. The chimera interfaces are denoted as I_1 and I_2 for the inner and outer problems, respectively, with unit normal vectors $\mathbf{n}_1$ and $\mathbf{n}_2$ pointing into the respective domains. Solid boundaries are also included in the conceptual scheme denoted as W_1 and W_2, respectively. The sources S are fully encompassed by the interface I_2. In the inner domain the wave equation is solved for the scattered field $\phi^{(1)}$, while in the outer domain the wave equation is solved for the overall field $\phi^{(2)}$. For simplicity, the walls are assumed to be rigid with vanishing normal derivative of the acoustic pressure. Far-field nonreflecting conditions are specified on the boundary F_2 of the outer domain.

With reference to Fig. 1, the acoustic potential in the inner domain is required to satisfy the wave equation $\mathcal{L}(\phi) = 0$. The potential ϕ is split into the scattered contribution $\phi^{(1)}$ and the incident contribution $\phi^{\text{FW-H}}$. The incident field satisfies the wave operator, apart a small residual value ε. Finally, imposing the continuity of pressure and its normal derivative at the chimera interface I_1, the inner problem is described by the following equations:

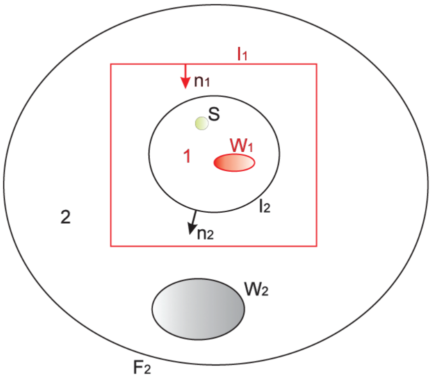

Fig. 1 Conceptual scheme of the chimera FW-H/FEM method.

$$\mathcal{L}(\phi^{(1)}; k, \tilde{\mathbf{U}}, \tilde{\rho}, \tilde{T}) = -\mathcal{L}(\phi^{\text{FW-H}}; k, \tilde{\mathbf{U}}, \tilde{\rho}, \tilde{T}) = \varepsilon \qquad (1)$$

$$\frac{\partial}{\partial n} p^{(1)} = -\frac{\partial}{\partial n} p^{(\text{FW-H})}_{W_1} \quad \text{on } W_1 \qquad (2)$$

$$p^{(1)} - p^{(2)} = -p^{(\text{FW-H})}_{I_1} \quad \text{on } I_1 \qquad (3)$$

$$\frac{\partial}{\partial n} p^{(1)} - \frac{\partial}{\partial n} p^{(2)} = -\frac{\partial}{\partial n} p^{(\text{FW-H})}_{I_1} \quad \text{on } I_1 \qquad (4)$$

The situation is specular for the outer domain in which the wave equation is solved for the overall acoustic potential $\phi^{(2)}$: namely,

$$\mathcal{L}(\phi^{(2)}; k, \tilde{\mathbf{U}}, \tilde{\rho}, \tilde{T}) = 0 \qquad (5)$$

$$\frac{\partial}{\partial n} p^{(2)} = 0 \quad \text{on } W_2 \qquad (6)$$

$$p^{(2)} - p^{(1)} = p^{(\text{FW-H})}_{I_2} \quad \text{on } I_2 \qquad (7)$$

$$\frac{\partial}{\partial n} p^{(2)} - \frac{\partial}{\partial n} p^{(1)} = \frac{\partial}{\partial n} p^{(\text{FW-H})}_{I_2} \quad \text{on } I_2 \qquad (8)$$

The FW-H solution is not, in general, a solution of the convected wave equation in the case of strong mean-flow gradients. Since it is not possible to compute the residual quantity ε in the inner domain, there is no way to avoid the introduction of a modeling error in the problem. Therefore, for the sake of the present work, the residual quantity ε is forced to zero. Although this splitting technique is limited to sufficiently low-speed helicopters, it serves the scopes of a noise scattering analysis though a propagation computed in the frequency domain. Different wave-splitting techniques are adopted in different fields of application; for instance, the case of sound generation in low-speed flow ducts for which a splitting of hydrodynamic and acoustic pressure fluctuations has been recently proposed by Schram [24].

Denoting $\xi^{(2)}_k$, $\eta^{(2)}_{k,i}$, and $\zeta^{(2)}_{k,ij}$ as the k FEM shape functions for the zeroth-, first-, and second-order derivatives of ϕ at the nodal locations of the chimera interface I_1 and reconstructed from the nodal values of grid 2, and vice versa for $\xi^{(1)}_k$, $\eta^{(1)}_{k,i}$, and $\zeta^{(1)}_{k,ij}$, the inner and outer problems can be cast in the following forms.

Inner problem:

$$\mathcal{L}(\phi^{(1)}; k, \tilde{\mathbf{U}}, \tilde{\rho}, \tilde{T}) = 0 \qquad (9)$$

$$ikn_i \frac{\partial \phi^{(1)}}{\partial x_i} - n_i \tilde{U}_j \frac{\partial^2 \phi^{(1)}}{\partial x_i \partial x_j} = -\frac{1}{\rho_a c_a \tilde{\rho}} \frac{\partial}{\partial n} p^{(\text{FW-H})}_{W_1} \quad \text{on } W_1 \qquad (10)$$

$$ik\phi^{(1)} - \tilde{U}_i \frac{\partial \phi^{(1)}}{\partial x_i} - \sum_k (ik\xi^{(2)}_k - \tilde{U}_i \eta^{(2)}_{k,i})\phi^{(2)}_k = -\frac{1}{\rho_a c_a \tilde{\rho}} p^{(\text{FW-H})}_{I_1} \quad \text{on } I_1 \qquad (11)$$

$$ikn_i \frac{\partial \phi^{(1)}}{\partial x_i} - n_i \tilde{U}_j \frac{\partial^2 \phi^{(1)}}{\partial x_i \partial x_j} - \sum_k (ikn_i \eta^{(2)}_{k,i} - n_i \tilde{U}_j \zeta^{(2)}_{k,ij})\phi^{(2)}_k = -\frac{1}{\rho_a c_a \tilde{\rho}} \frac{\partial}{\partial n} p^{(\text{FW-H})}_{I_1} \quad \text{on } I_1 \qquad (12)$$

Outer problem:

$$\mathcal{L}\,(\phi^{(2)}; k, \tilde{\mathbf{U}}, \tilde\rho, \tilde T) = 0 \tag{13}$$

$$n_i \frac{\partial \phi^{(2)}}{\partial x_i} = 0 \quad \text{on } W_2 \tag{14}$$

$$ik\phi^{(2)} - \tilde U_i \frac{\partial \phi^{(2)}}{\partial x_i} - \sum_k (ik\xi_k^{(1)} - \tilde U_i \eta_{k,i}^{(1)})\phi_k^{(1)} = \frac{1}{\rho_a c_a \tilde\rho}\, p_{I_2}^{(\text{FW-H})} \quad \text{on } I_2 \tag{15}$$

$$ikn_i \frac{\partial \phi^{(2)}}{\partial x_i} - n_i \tilde U_j \frac{\partial^2 \phi^{(2)}}{\partial x_i \partial x_J} - \sum_k (ikn_i \eta_{k,i}^{(1)} - n_i \tilde U_j \zeta_{k,ij}^{(1)})\phi_k^{(1)} = \frac{1}{\rho_a c_a \tilde\rho} \frac{\partial}{\partial n}\, p_{I_2}^{(\text{FW-H})} \quad \text{on } I_2 \tag{16}$$

and the radiation condition on F_2.

Since only one boundary condition per node can be imposed, a linear combination of the pressure and normal-derivative pressure continuity conditions can be imposed on each chimera interface. Furthermore, linear independent combinations have to be specified on the two interfaces in order to prevent the matrix singularity in the case of matching interfaces (adjacent grids).

In the present FEM implementation, only the case of propagation in a quiescent fluid is addressed. The method is verified against a simple two-dimensional prototype problem that is described in the following paragraphs. An application to a three-dimensional problem is presented in Sec. V.C.

A square domain ([−1.75:1.75] × [−1.75:1.75]) is discretized in 70 quad elements per direction. The chimera grids are obtained by removing 10 cells per direction in the middle of the square and patching the hole with a circular domain of radius 0.5 discretized with 78 constant boundary edges and 894 uniformly distributed triangles. To test the capability of the method to take into account the presence of a body in the inner domain, the case of a cylinder of radius 0.1 in the inner domain is also considered. A view of the two addressed grid topologies is shown in Fig. 2.

Three test cases are considered: 1) propagation in the free field, 2) propagation in the presence of a reflecting plane on the outer grid boundary $y = -1.75$, and 3) propagation in the presence of a reflecting plane on the outer grid boundary $y = -1.75$ and a cylinder in the inner domain. For tests 1 and 2, two Dirac sources of magnitude $1 + i$ and $-1 + i$ are located at (0.1, 0.1) and (−0.1, −0.1), respectively. For test 3, one Dirac source of magnitude $1 + i$ is located at the point (0.13, 0.13). All computations are carried out for the acoustic wave number $k = 10$ and using eight-point quadrangular and six-point triangular quadratic serendipity elements (see Figs. 8.9 and 8.15 of [25]).

Test 1 has a twofold goal: to verify the chimera capability without jump conditions at the interface, and to verify the wave-splitting technique with jump conditions. Three computations are performed: the first one using the Cartesian grid and considering two field sources in the computational domain (no-chimera), the second one using the chimera grid and considering two field sources in the computational domain (chimera/no-jump), and the third one using the chimera grid and prescribing jump conditions at the chimera interfaces (chimera/jump). The first computation provides a reference solution for a standard single domain computation with field sources introduced as Dirac functions at the right-hand side of the wave equation. The second computation relies on a two-domain splitting and a chimera coupling, but the sources are still introduced as Dirac functions at the right-hand side of the wave equation. Finally, the third computation is similar to the second one, but the Dirac sources are eliminated and substituted by equivalent jump conditions on the two chimera interfaces. All the jump conditions are computed analytically. Nonreflecting perfectly matched layer conditions are applied to the radiation boundaries. The real and imaginary parts of the acoustic pressure along a circular arc of radius 0.75 is plotted in Fig. 3. The chimera/no-jump and chimera/jump solutions are in perfect agreement, while the maximum relative L_0 difference with respect to the no-chimera solution is 3 and 1% for the real and imaginary parts, respectively.

The test 2 goal is to investigate the nonreflecting capabilities of the chimera interface. The same computations as in Test 1 are performed, but applying a rigid wall boundary condition on the $y = -1.75$ edge. Results are compared in Fig. 4. Again, a perfect agreement is found between chimera/no-jump and chimera/jump results, while the maximum relative L_0 difference with respect to the no-chimera solution is 1 and 3% for the real and imaginary parts, respectively. Contour plots of the acoustic field are shown in Fig. 5. Interestingly, the chimera jump conditions support the effective sound field in the outer domain and a virtual field in the inner domain that seems to recover the backreflected wave. Moreover, the backreflected wave can cross the chimera interfaces without spurious reflections.

The test 3 goal is to investigate the capabilities of the splitting method to take into account a wave reflection from bodies in the inner and outer domains. Computations are carried out by applying a rigid wall boundary condition on the $y = -1.75$ edge and a inserting a cylinder in the inner domain. Results obtained using a field source (chimera/no-jump) and jump conditions (chimera/jump) are compared in Fig. 6. Again, a perfect agreement is found between chimera/

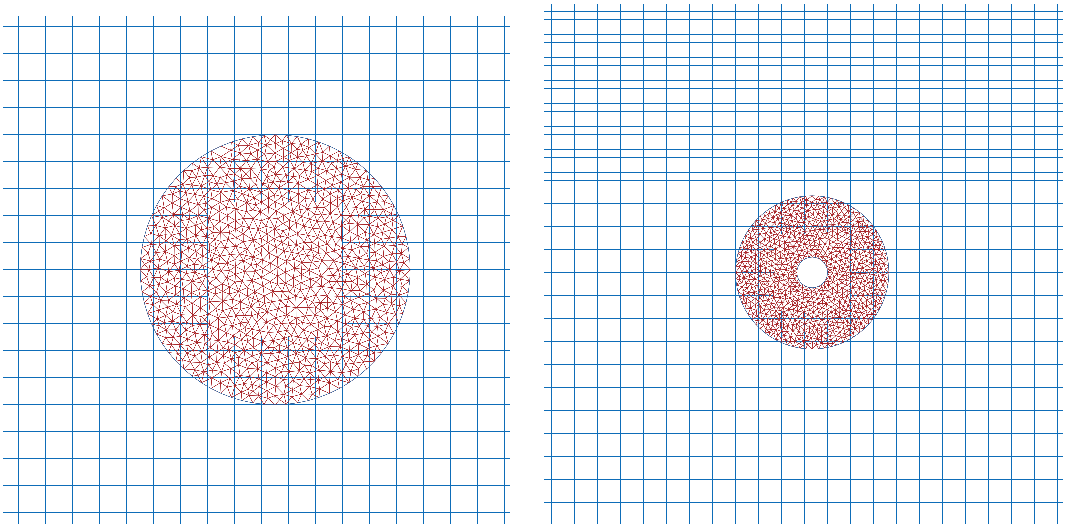

Fig. 2 Zoom view of the chimera region for the first grid topology considered (left) and full view of the second grid topology including a cylinder at the center of the computational domain (right).

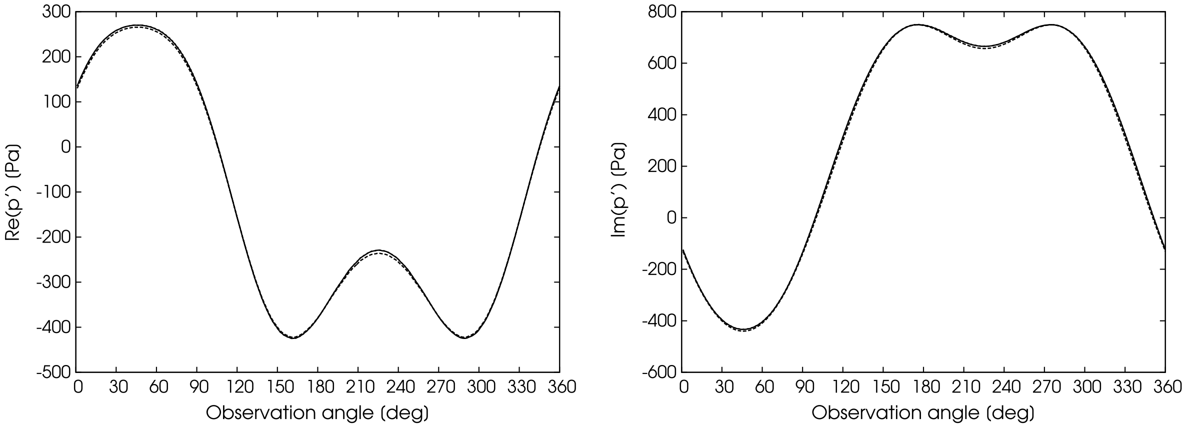

Fig. 3 Test 1. Comparison between no-chimera (dashed line), chimera/no-jump (dot line) and chimera/jump (line) results. Real (left) and imaginary (right) parts of the acoustic pressure along circular arc of radius 0.75.

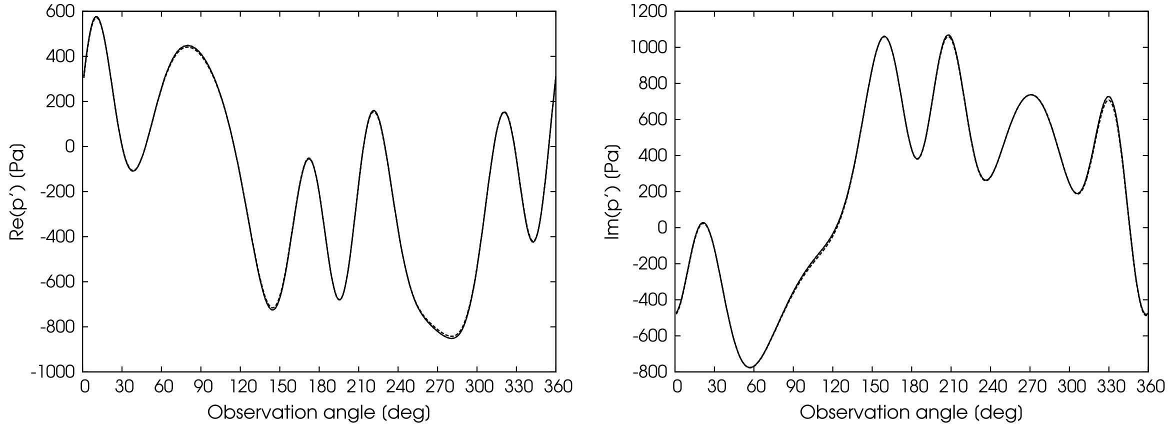

Fig. 4 Test 2. Comparison between no-chimera (dashed line), chimera/no-jump (dot line) and chimera/jump (line) results. Real (left) and imaginary (right) parts of the acoustic pressure along circular arc of radius 0.75.

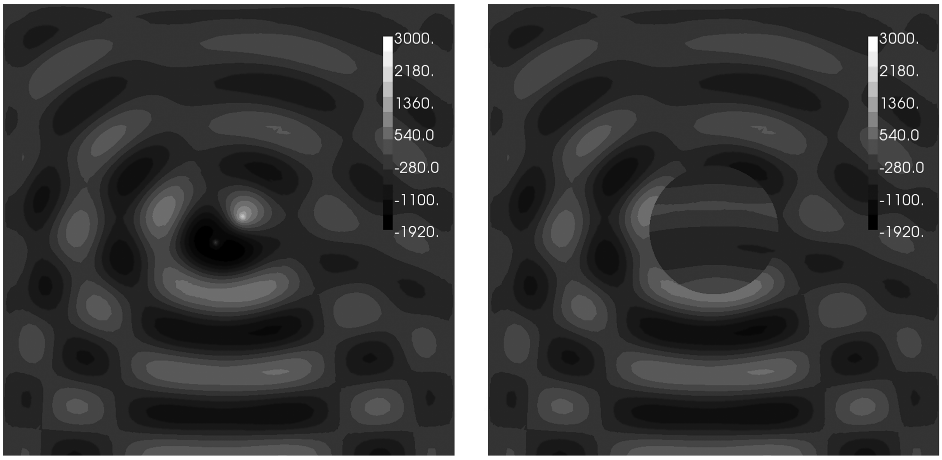

Fig. 5 Test 2. Contour plots of the real part of the acoustic pressure. Comparison between chimera/no-jump (left) and chimera/jump (right) results.

no-jump and chimera/jump results. Contour plots of the acoustic field are shown in Fig. 7.

IV. FRN Model

To compute the right-hand side of Eqs. (11), (12), (15), and (16), the FW-H computation must be carried out for each node on the chimera interface and on the embedded body. Furthermore, since the normal derivative of the acoustic pressure is computed by finite difference between two layers of numerical microphones, several thousands of microphones are easily reached for realistic problems. In the present section a simplified rotor noise model is described that allows the FW-H computational time to be reduced by a significant factor, while preserving an acceptable accuracy level. The model has been developed in view of real-time helicopter trajectory optimizations.

The FRN model is based on the classical idea of replacing the rotor blade by an equivalent distribution of chordwise compact sources. In the hypothesis of far-field and geometric compactness conditions, the chordwise pressure distribution p_r (see Fig. 8) can be approximated

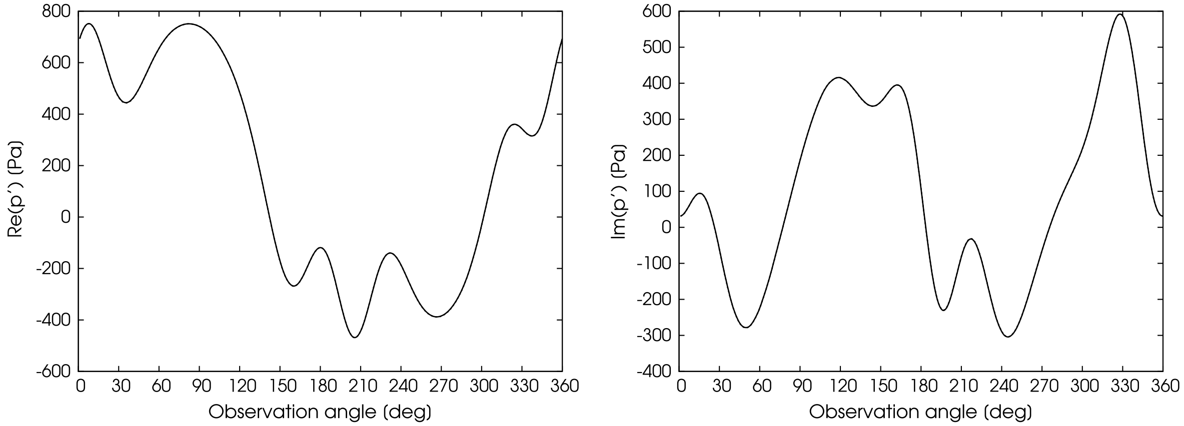

Fig. 6 Test 3. Comparison between chimera/no-jump (dot line) and chimera/jump (line) results. Real (left) and imaginary (right) parts of the acoustic pressure along circular arc of radius 0.75.

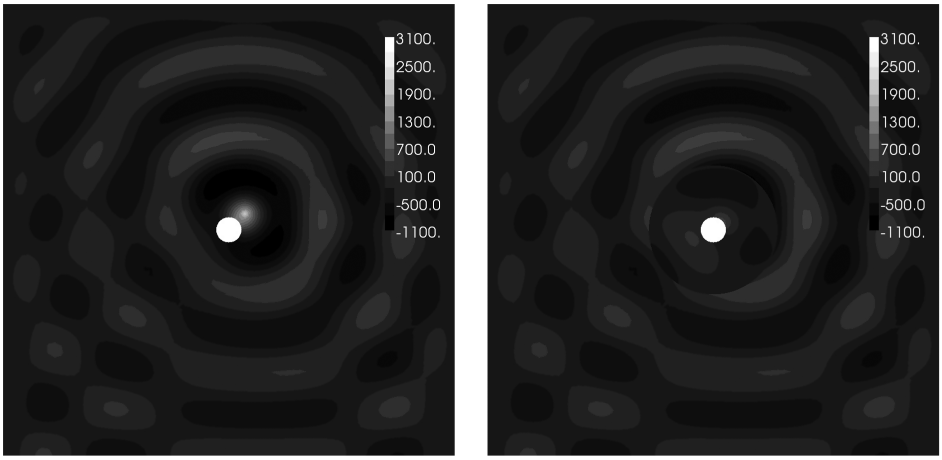

Fig. 7 Test 3. Contour plots of the real part of the acoustic pressure. Comparison between chimera/no-jump (left) and chimera/jump (right) results.

by a compact dipole through an equivalent constant pressure distribution p_{eq} that provides the same aerodynamic load. Moreover, in order to model the effect of flow displacement due to the blade motion (thickness noise), an equivalent monopole is introduced by considering a blade section of equivalent area, i.e., $A_{\mathrm{eq}} = A_r$. The blade is therefore modeled as a spanwise sequence of wedges that undergo the same rotational and pitching motion of the original blade. Deeper in detail, the procedure can be described as follows:

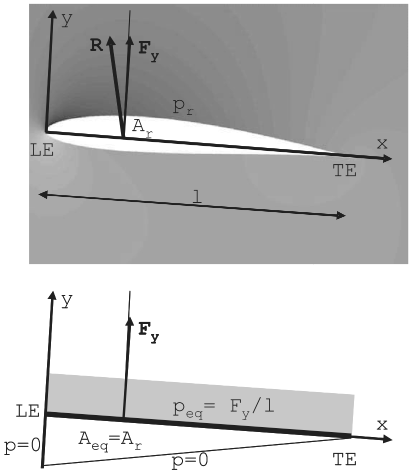

Fig. 8 Illustration of the FRN model concept. The component of the total aerodynamic force R along the normal direction *y* obtained by integration of the real blade pressure p_r is used to compute an equivalent constant pressure p_{eq} applied to a flat plate. A triangular section of area A_{eq} equal to the real section area A_r is created by adding two unloaded edges ($p = 0$).

1) A time sequence of pressure distributions over a structured blade grid is imported and for each time step the following operations are accomplished.

2) For each grid index in the spanwise direction, quadrangular elements are generated connecting the grid points on the leading edge with the grid points on the trailing edge.

3) The aerodynamic pressure force acting on each spanwise segment of the original blade is computed, and its projection on the normal direction to the corresponding quadrangular element is converted into a constant pressure distribution applied to the element.

4) For each grid index in the spanwise direction, the blade sectional area is computed and is used to define an equivalent triangular section. The acoustic equivalence of the triangular section with the original blade section relies on the classical theory of Ffowcs Williams and Hawkings [26].

V. Verification and Validation of the Isolated Rotor Noise Prediction

In this section computed noise levels for a helicopter in blade–vortex interaction (BVI) conditions are compared with available experimental data. This provides a validation of the unsteady aerodynamic and FW-H solution. Then results obtained by using the conventional FW-H approach are compared with those obtained by using the FRN model. This provides a verification of the FRN model for a relevant case. Finally, FRN results for the first two blade-passing frequency (BPF) harmonics are compared with results obtained by

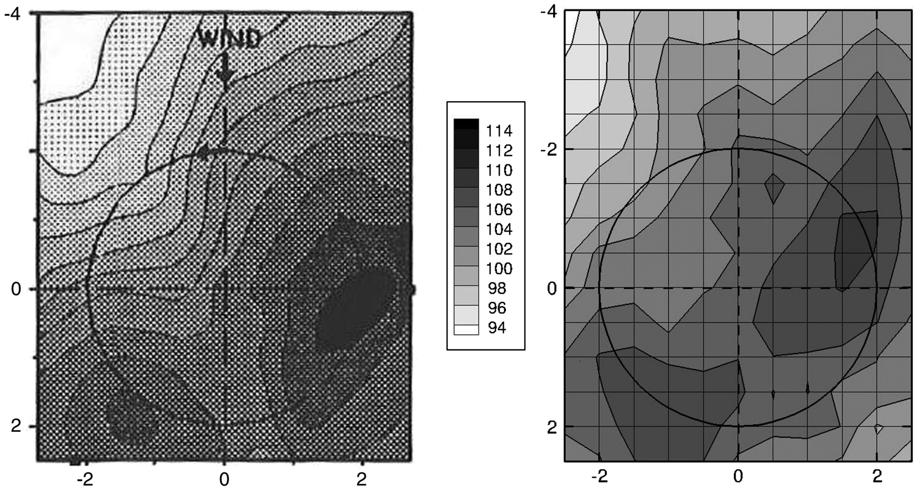

Fig. 9 OASLP over BPF harmonics 6 to 40. Comparison between experimental (left) and numerical (right) results.

using the frequency-domain FW-H/FEM approach. This provides a verification of the FW-H/FEM technique for a relevant case.

A. Validation of the Isolated Rotor Aeroacoustic Solution

To asses the compact source representation of the rotor blades, the test case 1333 of the HELINOISE [27] wind-tunnel test campaign is considered. This test case deals with an isolated rotor at an advance ratio $\mu = 0.15$ in a 6 deg descent flight, a condition characterized by the occurrence of strong BVI. The rotor is a 40% geometrically and dynamically scaled model of the four-bladed, hingeless BO-105 main rotor, having a radius $R = 2$ m and a solidity of 0.0077. The blades are rectangular with a root cutout of 0.035 m and a chord length $l = 0.121$ m. Each blade section consists of a NACA 23012 airfoil and has a linear twist of -8 deg. The nominal rotor operational speed is 1040, thus yielding an acoustic BPF of about 70 Hz.

The aerodynamic pressure distribution is predicted numerically using an aerodynamic BEM code [12]. The same blade kinematics measured during the test campaign is prescribed in the aerodynamic computation. Then the unsteady blade pressure and the blade kinematics are used to perform noise computations using the FW-H equation implemented in the code $Opty\partial B^{\mathrm{FWH}}$. Comparisons between numerical and experimental acoustic results are presented for two different ranges of frequencies. Contour plots of the noise levels on a rectangular carpet of microphones located 2.5 m below the rotor are shown in Fig. 9. It can be observed that the numerical approach is able to feature the BVI noise footprint. The validation of the aeroacoustic prediction is a secondary outcome of the present study, since the main focus is in the verification of the coupled FW-H/FEM method. Thus, these results are simply used as reference results for the verification of the FRN model.

B. Verification of the FRN Model

To verify the accuracy of the FRN model, comparisons between the conventional BEM/FW-H results, obtained by integrating directly the aerodynamic unsteady blade pressure, and the FRN/FW-H results are shown in Fig. 10. The overall sound pressure level (OASPL) carpet distributions in two frequency ranges show that even at the present small distance of the microphones (near field), both high- and low-frequency noise components are well predicted by the FRN model when both the loading and thickness noise terms are considered. Conversely, when only the loading noise term is considered, the prediction in the overall frequency range (BPF harmonics 1 to 40) is less accurate (Fig. 10b), in particular, at higher angles from the rotor axis, i.e., approaching the carpet boundaries. The accuracy loss is due to the low-frequency spectral components, as confirmed by the agreement between the noise footprints at higher

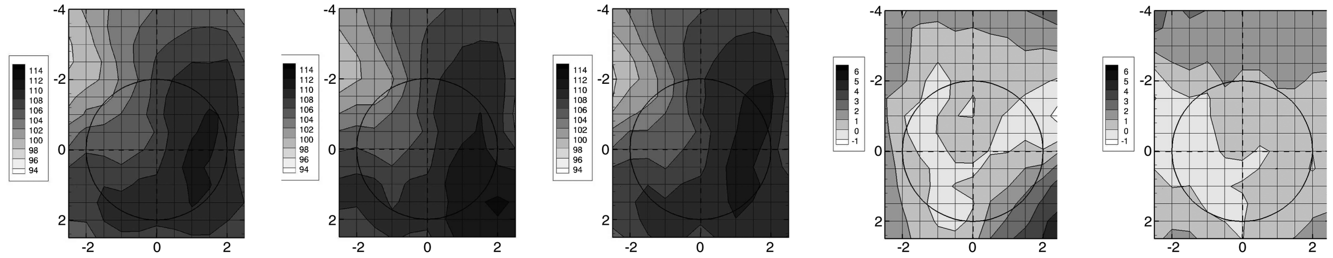

a) BEM **b) FRN: dip.** **c) FRN: dip. + mon.** **d) Δ dB: dip.** **e) Δ dB: dip. + mon.**

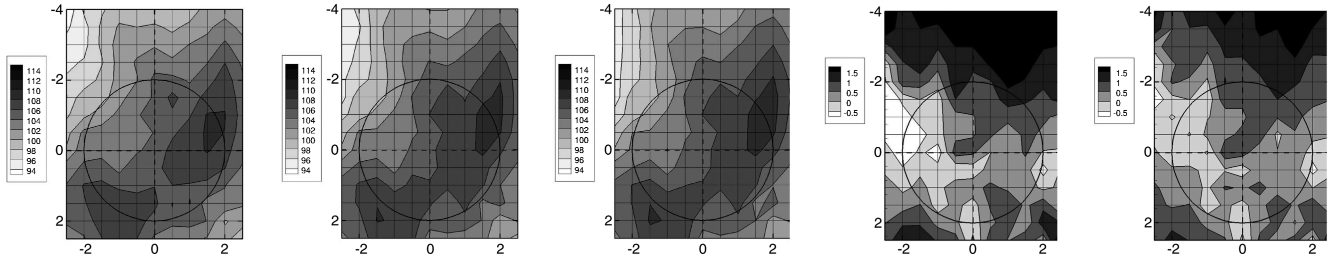

f) BEM **g) FRN: dip.** **h) FRN: dip. + mon.** **i) Δ dB: dip.** **j) Δ dB: dip. + mon.**

Fig. 10 OASPL over harmonics 1 to 40 (top) and 6 to 40 (bottom). Comparison between conventional BEM/FW-H results (labeled BEM) and FRN/FW-H results (labeled FRN).

Table 1 Comparison between conventional BEM/FW-H results and FRN/FW-H results OASPL results[a]

Method	Low frequency, dB	High frequency, dB
BEM/FW-H	106	103
FRN/FW-H (dipole)	108	104
ΔdB (dipole)	2	1
FRN/FW-H (dipole plus monopole)	107	104
ΔdB (dipole plus monopole)	1	1

[a] OASPL computed over harmonics 1 to 40 (low frequency) and 6 to 40 (high frequency), cumulated over the whole microphone carpet.

frequency shown in Figs. 10h and 10g. In general, the thickness noise contribution is even more important in the far field and, in particular, when the microphones are close to the rotor disk. Hence, when used for trajectory optimizations, the FRN model has to include the monopole component. The contour plots of the OASPL difference between the FRN/FW-H results and the BEM/FW-H results confirm the improvement due to the inclusion of the compact monopole term in the FRN model.

A further quantification of the accuracy of the FRN model can be made by comparing the OASPL averaged over the microphone carpet. The results for the overall (harmonics 1 to 40) and high-frequency (harmonics 6 to 40) regimes are gathered in Table 1. In the overall frequency regime the inclusion of the compact monopole in the FRN model reduces the error from 2 to 1 dB. In the high-frequency regime, the error is 1 dB for both the FRN formulations.

Finally, loading and thickness noise signals at one microphone location in the near field are plotted separately in Fig. 11. The comparison with the conventional FW-H results clearly shows that the FRN model is able to correctly predict both the loading and thickness noise contributions.

C. Verification of the FW-H/FEM Approach

To verify the full FW-H/FEM computational chain for a three-dimensional case, the free-field propagation of the first two BPF tones is computed in a volume and projected on a carpet of microphones, where it is compared with results obtained using the FW-H analogy applied directly to the same unsteady blade pressure field. The flight condition is the same as the one described in the previous subsections. Both the direct FW-H approach and the FW-H/FEM coupled approach are applied in fully free-field conditions. Since in both cases the FW-H computation makes use of the FRN model and it is carried out setting the helicopter translational velocity to zero (the Doppler effects are neglected), the only differences expected between the two sets of results are due to the error introduced by the chimera and FEM discretization and to a lack of convergence of the linear system solution.

Figure 12 shows the topology of the CAA grids used for the case of rotor noise radiation in the presence of the helicopter fuselage and buildings. The details of this computation are described in Sec. VI.

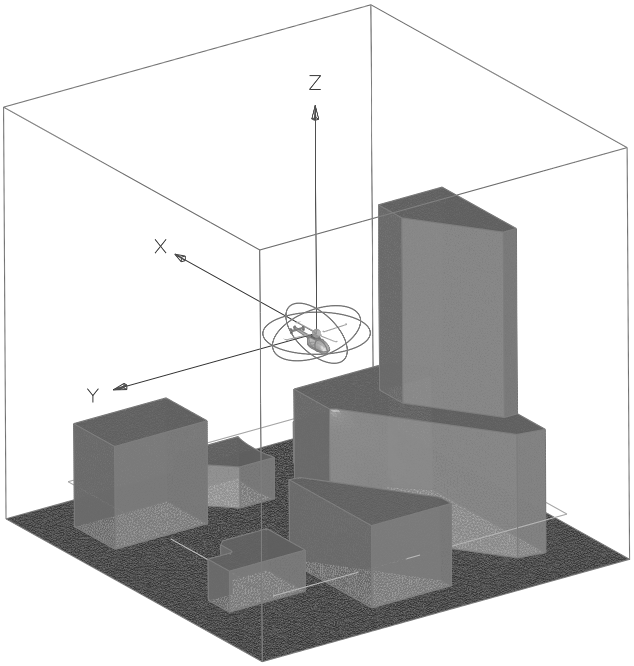

Fig. 12 CAA mesh topology for the case of helicopter noise propagation in an urban area. The helicopter rotor center is located at an altitude from the ground level of 12.5 m. The same bounding box is also used for the verification of the FW-H/FEM approach in the absence of any solid surface (ground, buildings and helicopter fuselage). The edges of a microphone carpet located at an altitude of 2.5 m are also plotted.

For the sake of the present verification, a CAA mesh with the same bounding box and chimera interface is used, and it is obtained by removing the fuselage and the buildings from the full mesh. Coincident chimera interfaces are used, having the shape of an ellipsoid (only the three generating ellipses are plotted for clarity) that encompasses both the rotor and the fuselage. The inner and outer volumes are discretized with tetrahedral cells. The minimal edge in the far-field corresponds to about 10 points per acoustic wavelength at the second BPF, while in the fuselage region the average cells size is reduced by a factor of 5. The edges of the microphone carpet used to compare the direct FW-H results and the FW-H/FEM results are also plotted in the figure. This is a square of edge equal to $10R$, with R denoting the rotor radius, and it is located at $z = -5R$, the origin of the reference system being on the rotor midpoint.

The contour plots of the sound pressure level (SPL) on the microphone carpet computed for the first and second BPF are shown in Fig. 13. Comparing the reference FW-H and the FW-H/FEM results shows that the noise footprint is globally well predicted by the FW-H/FEM method. However, differences occur, which are due to the several discretization errors involved in the two computations. In particular, the one associated with the computation of the normal

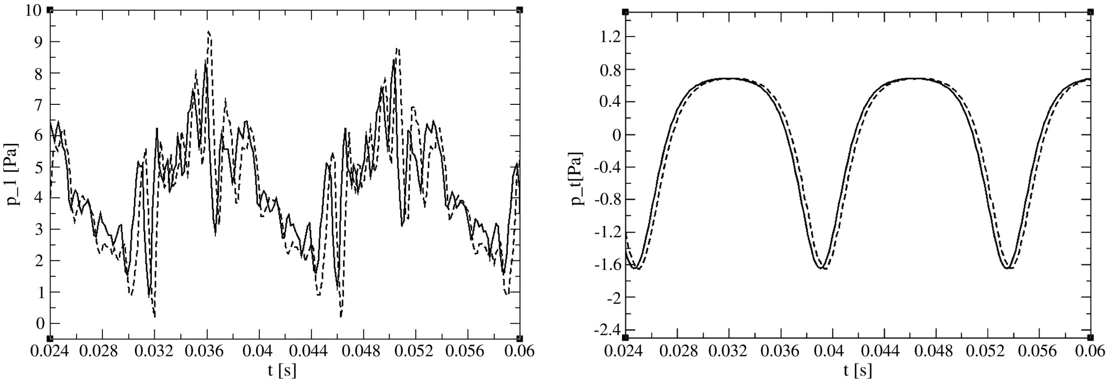

Fig. 11 Comparison between pressure signals obtained using the BEM pressure distribution and the FW-H analogy (solid line), and using the FRN model (dashed line). Loading noise on the left, thickness noise on the right. Microphone located at the point (−3 m, −4 m, −2.5 m).

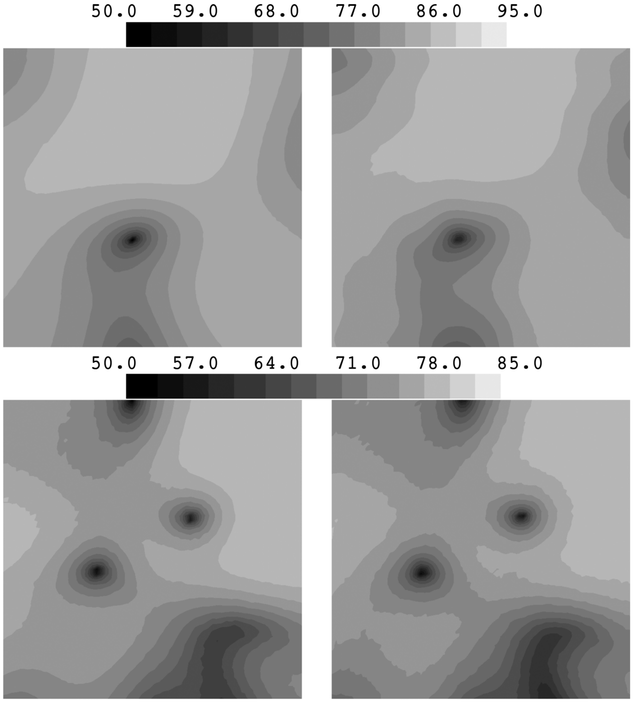

Fig. 13 SPL contour plots on the microphone carpet. Comparison between FW-H (left) and FW-H/FEM (right) results for the first (top) and second BPF (bottom). The FW-H/FEM results have been obtained in the absence of any reflecting obstacle.

derivative of the acoustic pressure on the chimera interface has a significant effect, as shown hereafter. In the present implementation, in fact, a first-order one side finite difference formula is used.

A quantitative comparison of the results is shown in Fig. 14, where the SPL along the carpet diagonal is plotted. The FW-H results are compared with the FW-H/FEM results obtained for two values of the distance δ between the two layers of microphones on the chimera interface. The smaller distance provides the more accurate results: for the first BPF, the maximum error is 1 dB, whereas for the second BPF, the maximum error is 2 dB. Globally, the verification of the FW-H/FEM method for the specific practical case addressed in this work can be considered satisfactory.

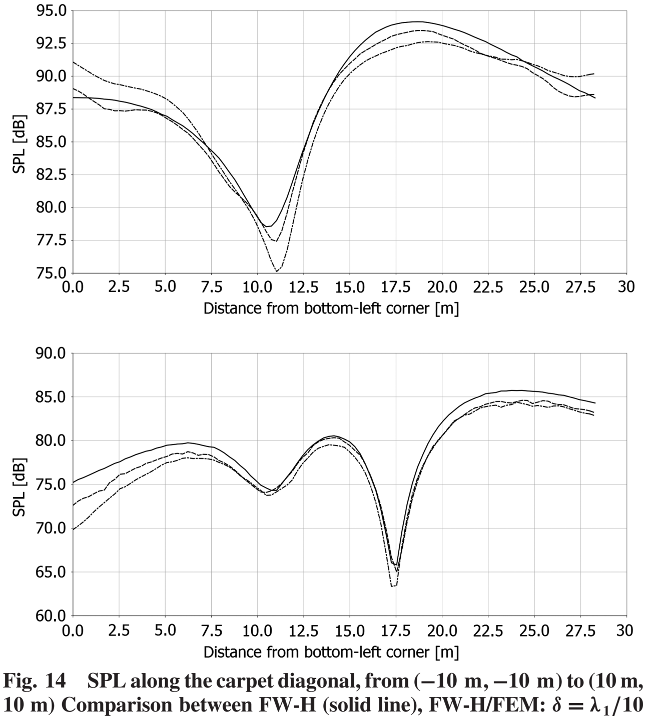

Fig. 14 SPL along the carpet diagonal, from (−10 m, −10 m) to (10 m, 10 m) Comparison between FW-H (solid line), FW-H/FEM: $\delta = \lambda_1/10$ (dashed line) and FW-H/FEM: $\delta = \lambda_1/40$ (dash-dotted line) results for the first (top) and second BPF (bottom). The quantity λ_1 denotes the acoustic wavelength for the first BPF.

VI. Simulation of Helicopter Noise Propagation in an Urban Area

In this section illustrative results are reported, showing the acoustic pressure levels on the surface of a realistic set of buildings. Computations have been performed using only perfectly rigid surfaces. The mesh topology is shown in Fig. 12. The overall modeled domain has an edge of 25 m, corresponding to 62.5 m in full scale. The computational mesh consists of about 1.2×10^6 nodes and 6.7×10^6 tetrahedral cells. The chimera interfaces (perfectly matching) consist of about 2.2×10^3 nodes each, and the number of nodes on the fuselage is about 2.6×10^3. Overall, the noise signals are computed at about 14×10^3 microphones, i.e., twice the number of overall microphones for the finite difference evaluation of the pressure normal derivative. Reducing the residue of the FEM linear system of five orders of magnitude with respect to the initial residue corresponding to a zero solution, the whole computation requires about 3 h for the first frequency run and 2.5 h for successive frequency runs, using only one processor of a laptop equipped with a 2.5 GHz Q9300 Intel CPU. A significant time is used for input/output operations, considering that the full amount of data produced by the first frequency run and used for successive runs is about 4 GB, only 600 MB of which being used for to the solution file.

Figure 15 shows the noise print on the buildings computed for the first and second BPF. In addition, the rotor wake is plotted, showing the occurrence of BVI. The pressure field on one of the two chimera interfaces is shown in translucent colors. It can be observed that for the first BPF, a number of four acoustic lobes (positive and negative), one for each rotor blade, take place on the chimera interface, whereas eight lobes occur for the second BPF. This is a well-known aeroacoustic property of rotating machines.

Three main modeling assumptions have been made in the present work that can reduce the generality of the approach. The first one is related to the spectral content of BVI noise, which is characterized by high-frequency tones. The highest frequency that can be simulated using the same computational platform and the same urban assembly model cannot exceed the 4th BPF. Higher harmonics can be achieved through memory-shared parallel computations on cluster calculators. Analogously, more extended urban assemblies can be easily analyzed only for the first BPF, as relevant in the absence of BVI.

The second assumption is the sound propagation in a quiescent fluid, but this is mainly related to the specific software implementation and not to modeling limitations. Developments will be undertaken in the future in order to include the mean-flow convective effects in the wave-splitting technique. To a certain extent, which is difficult or even impossible to be a priori quantified, the mean-flow refraction effects can be also taken into account by the FEM propagation model, but only those occurring in the outer domain due to time-average atmospheric gradients and large-scale building-induced flow nonuniformities. Notwithstanding, two deficiencies of the approach will be not cured: the capability of the propagation model to account for stochastic convective/refractive effects due to atmospheric turbulence [28,29], and the capability of the FW-H approach to account for mean-flow refraction effects in the source region. More generally, the first limitation would be overcome through a time-domain propagation model, and the second one would be overcome extracting the pressure fluctuation at the chimera interface from an unsteady compressible CFD solution instead of using the results of a FW-H computation.

The third assumption is related to the helicopter movement and the Doppler effects. It has been assumed that the helicopter flight distance over one acoustic period is sufficiently small compared with a characteristic dimension of the problem. For this specific case, for instance, the flight distance is equal to about the 20% of the rotor radius for the first BPF harmonic. While the first two limitations are

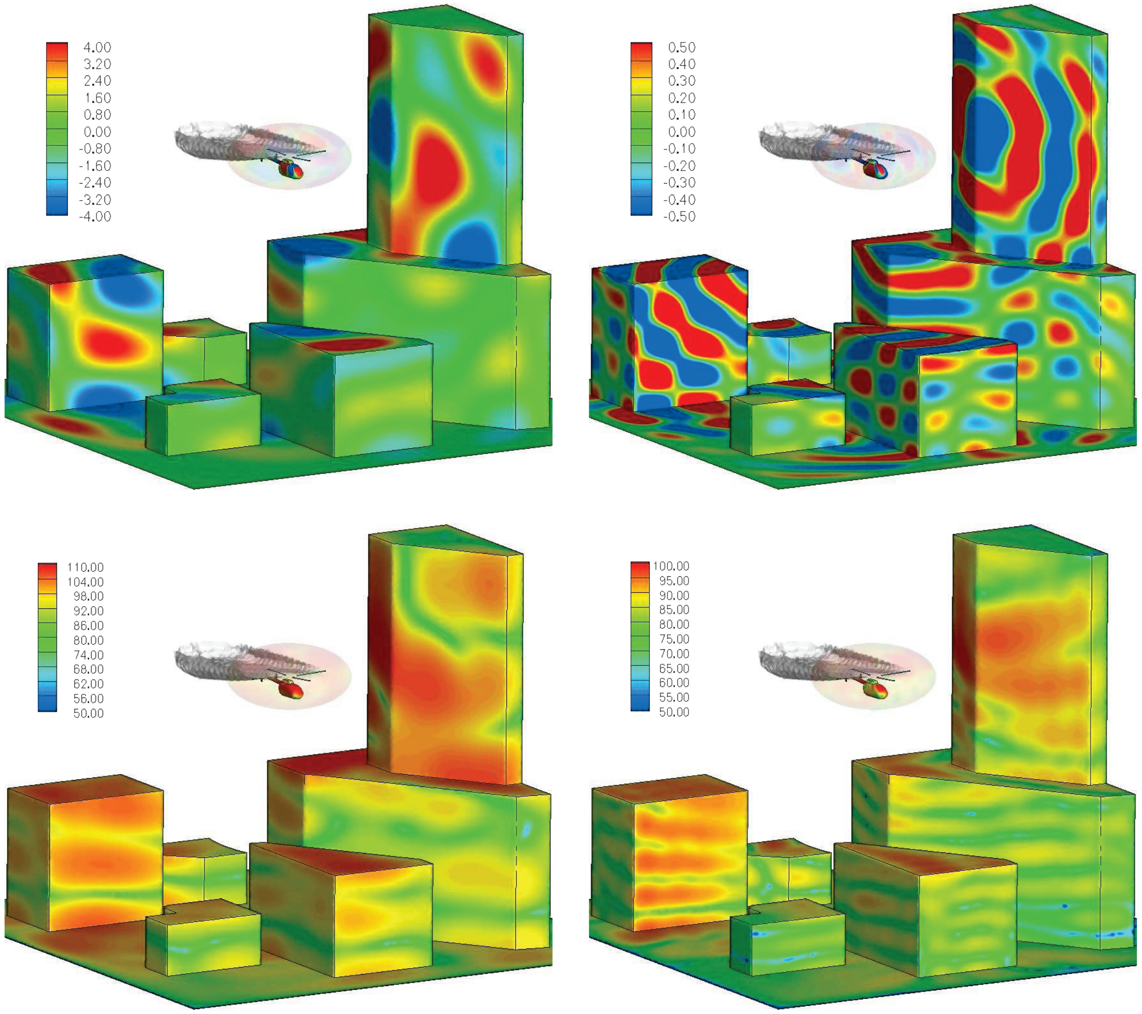

Fig. 15 Noise print on the surface of a building set. Contour plots of the real part of the acoustic pressure [Pa] on the top and of the SPL on the bottom. first BPF on the left and second BPF on the right.

related to contingent circumstances, the third one constitutes the main limitation of the present numerical approach for the prediction of helicopter noise propagation in urban areas.

VII. Conclusions

This paper constitutes a successful attempt to couple a time-domain FW-H rotor noise generation model with a frequency-domain FEM propagation model. The hybrid FW-H/FEM technique exploits an overlapping grid modality to split the propagation problem into an inner and outer problem, matched through jump conditions accounting for the rotor noise. In the present implementation, the mean-flow effects are not taken into account, but an extension to sound propagation in a nonuniform and sufficiently smooth mean flow is feasible. A second outcome of the present study is the implementation of a simplified rotor noise model that is based on the analogy between a blade and a spanwise distribution of compact dipoles and monopoles. The model allows the CPU time to be reduced by a significant factor, while preserving an acceptable accuracy level, both in the near and far fields and for a broad frequency range. The present computational chain, involving a BEM free-wake aerodynamic prediction, a FW-H analogy applied to an acoustically equivalent blade and the FEM sound propagation at prescribed frequencies in a complex environment can be used for helicopter noise predictions in urban areas and on the decks of ships.

Acknowledgment

The fast rotor noise model has been developed for real-time helicopter trajectory optimizations to be carried out in the framework of the Clean Sky—Green Rotorcraft project funded by the European Commission.

References

[1] Moorhouse, A., Waddington, D., and Adams, M., "DEFRA NANR45: Proposed Criteria for the Assessment of Low Frequency Noise Disturbance," University of Salford, Salford, England, U.K., 2005.

[2] "Builders Guide: Mitigating Aircraft Noise in New Residential Construction," Metropolitan Council, TR 35-06-019, March 2006.

[3] Shaw, G. B., and Trost, R. P., "Statistical Analysis of Hearing Loss Among Navy Personnel," Centers for Naval Analyses, TR CRM D0011228.A2/Final, Feb. 2005.

[4] Gennaretti, M., and Testa, C., "A Boundary Integral Formulation for Sound Scattered by Elastic Moving Bodies," *Journal of Sound and Vibration*, Vol. 314, Nos. 3–5, 2008, pp. 712–737. doi:10.1016/j.jsv.2008.01.028

[5] Di Francescantonio, P., "The Prediction of the Sound Scattered by Moving Bodies," *16th CEAS/AIAA Aeroacoustics Conference*, June 1995.

[6] Schram, C., Beriot, H., Roger, M., Reese, H., and Carolus, T., "On the Importance of Near-Field Terms in the Assessment of Acoustic Installation Effects for Ducted Low-Mach Number Fans," AIAA Paper 2009-3334, May 2009.

[7] Casalino, D., Genito, M., and Visingardi, A., "Numerical Analysis of Airframe Noise Scattering Effects in Tilt-Rotor Systems," *AIAA Journal*, Vol. 45, No. 4, 2007, pp. 751–759. doi:10.2514/1.24605

[8] Farassat, F., "Introduction to Generalized Functions with Applications in Aerodynamics and Aeroacoustics," NASA TP 3428, 1994.

[9] Taghizad, A., Verbeke, C., and Desopper, A., "Aerodynamic Perturbations Encountered by a Helicopter Landing on a Ship—Effects on the

Helicopter Flight Dynamics," *Fluid Dynamics Problems of Vehicle Operating Near or in the Air-Sea Interface*, Research and Technology Organization, Neuilly-sur-Seine, France, Oct. 1998.

[10] Tattersall, P., Albone, C. M., Soliman, M. M., and Allen, C. B., "Prediction of Ship Air Wakes over Flight Decks using CFD," *Fluid Dynamics Problems of Vehicle Operating near or in the Air-Sea Interface*, Research and Technology Organization, Neuilly-sur-Seine, France, Oct. 1998.

[11] Wadcock, A. J., Yamauchi, G. K., Heineck, J. T., Silva, M. J., and Long, K. R., "PIV Measurements of the Wake of a Tandem-Rotor Helicopter in Proximity to a Ship," *AHS 4th Decennial Specialist's Conference on Aeromechanics*, AHS International, Alexandria, VA, Jan. 2004.

[12] Visingardi, A., D'Alascio, A., Pagano, A., and Renzoni, P., "Validation of CIRA's Rotorcraft Aerodynamic Modelling System with DNW Experimental Data," *22nd European Rotorcraft Forum*, Brighton, England, U.K., 1996.

[13] Banerjee, P. K., and Morino, L., *Developments in Boundary Element Methods*, Vol. 6, Elsevier Applied Science, Barking, England, U.K., 1990.

[14] Gennaretti, M., and Bernardini, G., "A Novel Potential Flow Boundary Integral Formulation for Helicopter Rotors in BVI Conditions," AIAA Paper 2005-2924, May 2005.

[15] Farassat, F., and Succi, G. P., "The Prediction of Helicopter Discrete Frequency Noise," *Vertica*, Vol. 7, No. 4, 1983, pp. 309–320.

[16] Casalino, D., "An Advanced Time Approach for Acoustic Analogy Predictions," *Journal of Sound and Vibration*, Vol. 261, No. 4, 2003, pp. 583–612.
doi:10.1016/S0022-460X(02)00986-0

[17] Astley, R. J., and Eversman, W., "A Finite Element Method for Transmission in Non-Uniform Ducts Without Flow: Comparison with the Method of Weighted Residuals," *Journal of Sound and Vibration*, Vol. 57, No. 3, 1978, pp. 367–388.
doi:10.1016/0022-460X(78)90317-6

[18] Casalino, D., "Benchmarking of Different Wave Models for Sound Propagation in Non-Uniform Flows," *Procedia Engineering*, Vol. 6, March 2010, pp. 163–172.

[19] Casalino, D., Roger, M., and Jacob, M., "Prediction of Sound Propagation in Ducted Potential Flows Using Green's Function Discretization," *AIAA Journal*, Vol. 42, No. 4, 2004, pp. 736–744.
doi:10.2514/1.1315

[20] Casalino, D., and Barbarino, M., "A Stochastic Method for Airfoil Self-Noise Computation in Frequency-Domain," AIAA Paper 2010-3884, June 2010.

[21] Pierce, A. D., "Wave Equation for Sound in Fluids with Unsteady Inhomogeneous Flow," *Journal of the Acoustical Society of America*, Vol. 87, No. 6, 1990, pp. 2292–2299.
doi:10.1121/1.399073

[22] Casalino, D., and Barbarino, M., "Turbofan Aft Noise Radiation: Progress Towards a Realistic CAA Simulation," AIAA Paper 2008-2882, May 2008.

[23] Casalino, D., Barbarino, M., Genito, M., and Ferrara, V., "Hybrid Empirical/Computational Aeroacoustics Methodology for Rocket Noise Modeling," *AIAA Journal*, Vol. 47, No. 6, June 2009, pp. 1445–1460.
doi:10.2514/1.38634

[24] Schram, C., "A Boundary Element Extension of Curle's Analogy for Non-Compact Geometries at Low-Mach Numbers," *Journal of Sound and Vibration*, Vol. 322, 2009, pp. 264–281.
doi:10.1016/j.jsv.2008.11.011

[25] Zienkievicz, O. C., and Taylor, R. L., *The Finite Element Method*, Vol. 1, Butterworth-Heinemann, Oxford, 2000.

[26] Ffowcs Williams, J. E., and Hawkings, D. L., "Sound Generated by Turbulence and Surfaces in Arbitrary Motion," *Philosophical Transactions of the Royal Society of London, Series A: Mathematical and Physical Sciences*, Vol. 264, No. 1151, 1969, pp. 321–342.
doi:10.1098/rsta.1969.0031

[27] Splettstoesser, W. R., Junker, B., Schultz, K.-J., Wagner, W., Weitemeier, W., Protopsaltis, A., and Fertis, D., "The HELINOISE Aeroacoustic Rotor Test in the DNW. Test Documentation and Representative Results," DLR, German Aerospace Center, TR 93-09, Dec. 1993.

[28] Lam, Y. W., "Ground and Meteorological Effects on Sound Propagation in the Atmosphere—Predictions and Measurements," *International Journal of Acoustics and Vibration*, Vol. 5, No. 3, 2000, pp. 135–139.

[29] Lam, Y. W., "An Analytical Model for Turbulence Scattered Rays in the Shadow Zone for Outdoor Sound Propagation Calculation," *Journal of the Acoustical Society of America*, Vol. 125, No. 3, 2009, pp. 1340–1350.

J. Astley
Associate Editor